Fall 2021

A Study on the Relationship of Arctic Oscillation with Atmospheric Rivers and Snowpack in the Western United States Using Forty-Year Multi-Platform Dataset

Samuel Liner
San Jose State University

A STUDY ON THE RELATIONSHIP OF ARCTIC OSCILLATION WITH ATMOSPHERIC RIVERS AND SNOWPACK IN THE WESTERN UNITED STATES USING FORTY-YEAR MULTI-PLATFORM DATASET

A Thesis

Presented to

The Faculty of the Department of Meteorology and Climate Science

San José State University

In Partial Fulfillment

of the Requirements for the Degree

Master of Science

by

Samuel Liner

December 2021

The Designated Thesis Committee Approves the Thesis Titled

A STUDY ON THE RELATIONSHIP OF ARCTIC OSCILLATION WITH ATMOSPHERIC RIVERS AND SNOWPACK IN THE WESTERN UNITED STATES USING FORTY-YEAR MULTI-PLATFORM DATASET

by
Samuel Liner

APPROVED FOR THE DEPARTMENT OF METEOROLOGY AND CLIMATE SCIENCE

SAN JOSÉ STATE UNIVERSITY

December 2021

Sen Chiao, Ph.D. Department of Meteorology and Climate Science

Ju-Mee Ryoo, Ph.D. NASA Ames Research Center, Atmospheric Science Branch, Science and Technology Corporation

Craig Clements, Ph.D. Department of Meteorology and Climate Science

ABSTRACT

A STUDY ON THE RELATIONSHIP OF ARCTIC OSCILLATION WITH ATMOSPHERIC RIVERS AND SNOWPACK IN THE WESTERN UNITED STATES USING FORTY-YEAR MULTI-PLATFORM DATASET

by Samuel Liner

Atmospheric rivers (ARs) are affected by large-scale climate variability. We investigate how ARs and snowpack are shaped by arctic oscillation (AO) by examining the synoptic conditions and characteristics of ARs and snowpack in the different phases of AO using forty years (1980-2019) of Integrated Multi-satellite Retrievals for Global Precipitation Measurement (IMERG) data, Modern-Era Retrospective analysis for Research and Applications, Version 2 (MERRA2) reanalysis data, and in-situ observation data over the eastern Pacific and western U.S. region. More precipitation is found in lower latitudes during negative AO months and farther north in latitude during positive AO months. These are associated with wavelike synoptic patterns in negative AO months while more straight-type synoptic patterns in positive AO months. The AR characteristics are also modulated by the different phase of AO: lower (higher) integrated water vapor transport and total precipitation, shorter (longer) duration of ARs, and less (more) ARs per month were more likely found during positive AO (negative AO) months with regional variability. Finally, snow water equivalent (SWE) tends to be reduced in positive AO phase and in high temperature condition, especially in the recent years, although the robust relationship remains unclear for long-term period. These findings highlight how the characteristics of local extreme weather during ARs can be shaped by large-scale climate variability.

ACKNOWLEDGEMENTS

I would like to take this opportunity to thank everyone involved in helping me to get here. First to my advisor Dr. Sen Chiao for giving me the opportunities and backing I needed to complete my thesis at SJSU. Next, I would especially like to express my appreciation to my mentor, Dr. Ju-Mee Ryoo, whose guidance and assistance greatly aided me through my research and writing process. I'd also like to thank my other committee member, Dr. Craig Clements, for teaching and counseling me while I was at SJSU. Finally, to my family, friends, and fellow classmates, whose encouragement, inspiration, and support has really made this achievement possible. I would also like to acknowledge NASA-Ames and the Center for Applied Atmospheric Research in Education (CAARE) for funding some of this research and Jonathan Rutz for his atmospheric river database.

TABLE OF CONTENTS

LIST OF TABLES

LIST OF FIGURES

1. Introduction

Atmospheric rivers (ARs) are narrow bands of enhanced integrated water vapor transport (IVT), which typically transfers moisture from the tropics and subtropics into the higher midlatitudes (Zhu and Newell 1998) as shown in Fig. 1. ARs generally are associated with extratropical cyclones and proceeded by a low-level jet stream but can be measured and categorized by their IVT and characterized as having widths no more than 400-500 kilometers wide, wind speeds in the lowest 2 kilometers of the atmosphere that are larger than 12.5 meters per second and concentrations of integrated water vapor (IWV) of at least 2 centimeters (Ralph and Dettinger 2011). Measurements of these AR characteristics can be applied to develop techniques that are used to help detect ARs (Guan and Waliser 2015). These meteorological phenomena occur all around the globe, but much of the focus has been given in the eastern Pacific Ocean where they are the cause of much of the extreme winter weather events in California and the Pacific Northwest (Dettinger et al. 2011) in Northern Hemisphere wintertime. Additionally, ARs are important to California's water resources, contributing up to fifty percent of the state's annual precipitation and streamflow (Dettinger et al. 2011). Understanding the influence of ARs is also critical to have accurate estimates of snowpack in the Western United States (Goldenson et al. 2018; Guan et al. 2016).

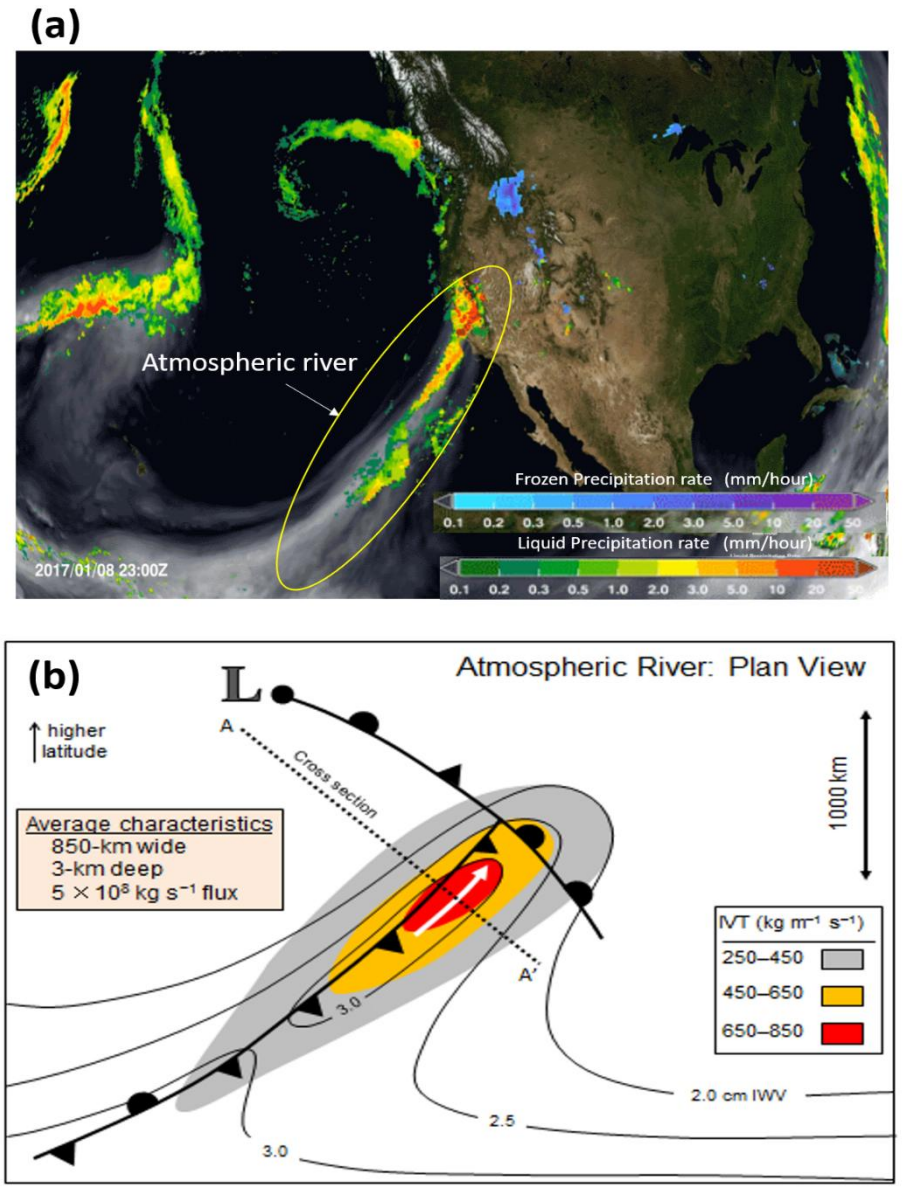

Fig. 1. (a) The example of precipitation associated with the AR, striking the western U.S. on January 8, 2017, 23 UTC (GPM precipitation; figure credit: NASA Goddard Space Flight Center (2017)). (b) Schematic plan view of the structure and strength of an AR (figure is adapted from Ralph et al. (2017) and found in © American Meteorological Society (2020)).

In the last three decades the study of atmospheric rivers as an area of research has grown exponentially starting with Newell et al. (1992). Through reanalysis and satellite data most studies have only identified ARs going back to 1998 (e.g., Guan et al. 2013; Neiman et

al. 2008; Ryoo et al. 2015). Model simulations have been conducted since 1982 (Goldenson et al. 2018) but no extensive analysis has been done on the IVT reanalysis data available. Research that has been done since 1998 have made the characteristics of ARs become clearer due to the advent of Special Sensor Microwave Imager (SSM/I) which has provided extensive integrated water vapor measurements across the globe, especially over the ocean where it was previously not possible to measure (Ralph and Dettinger 2011). ARs are frequently associated with extratropical cyclones as well as so called “bomb cyclones” (Zhu and Newell 1994), when the center pressure of a cyclone falls extremely rapidly and occur about 40-50 times per year. Furthermore, although atmospheric rivers only cover about ten percent of the globe longitudinally, they transport up to ninety percent of poleward water vapor (Newell et al. 1992; Zhu and Newell 1994; Zhu and Newell 1998).

Much of what determines an AR’s impact depends on where it makes landfall. Other than the observed characteristics, such as more landfalling ARs in the Pacific Northwest than northern California or southern California, there are geographical differences in moisture and elevation among these regions. When atmospheric rivers do make landfall, they share some features including a ridge centered onshore, a trough offshore, and localized warming in the lower troposphere (Harris and Carvalho 2018). In the Southern California area, higher areas of moisture that are connected to atmospheric rivers develop farther toward the equator and the east, in addition to appearing days earlier, implying less variability in different scenarios (Harris and Carvalho 2018). Geographical differences of ARs are also based on terrain of the area. Since water vapor transported in ARs are lower in the

atmosphere (under ~700 hPa) it is especially subject to orographic lifting, which is when moist air flows from lower terrain to higher terrain causing the air to cool and form clouds, producing precipitation (Ralph et al. 2013). From this it can be concluded that the location of the AR landfall is closely associated with the type of terrain which in turn influences how much water vapor falls as precipitation and how far inland the AR's influence reaches (Ryoo et al. 2020). Because of this it has been observed that the number of ARs that reach farther into the interior is largest in the Pacific Northwest, especially over lower elevation areas, while fewer ARs make it over the High Sierra Nevada mountains and into the Great Basin (Rutz et al. 2014).

Studies have demonstrated the importance of atmospheric rivers and snowpack in the Sierra Nevada mountains and therefore the water resources of California and the impacts of drought and flooding (Ralph et al. 2013 and Dettinger. 2013). The actual contribution of ARs to the snowpack in California depends on whether the ARs are landfalling (Dettinger et al. 2011). An increased number of atmospheric rivers can also influence snowpack when there are so called rain-on-snow (ROS) events, which was when precipitation as rain fell onto existing snowpack. When an ROS event occurs during an AR, air temperature is about 2 degrees Celsius higher than the average and there is a snow water equivalent loss of about 0.7 centimeters per day (Guan et al. 2016). ROS and AR events occurring in the different locations can have opposing effects on snowpack as shown in Goldenson et al. (2018) where there was an increase in snowpack in the Sierra Nevada Mountains and a decrease in snowpack in the Cascade Mountain Range.

Large-scale climate variability modulates different meteorological conditions that fluctuate frequently, demonstrating their possible linkages to ARs. There are several climate indices such as El Niño-Southern Oscillation (ENSO), Arctic Oscillation (AO), Pacific/North American Teleconnection Pattern (PNA), among others and can provide a general idea of how weather might behave in particular regions. ENSO strengthens or weakens surface winds over the ocean which typically increases the amount of precipitation in some regions and decreases it in other regions. Both AO and PNA deal with changes in atmospheric pressure over the land and the ocean in the Northern Hemisphere. Ryoo et al. (2013) showed that northwestern U.S. precipitation is highly modulated by the ENSO through the change in the location and intensity of the subtropical upper-level jet and moisture transport pathways. However, there is no significant correlation between AR measurements and sea surface temperatures (SST), meaning there is no significant correlation between El Niño Southern Oscillation and atmospheric rivers in the Pacific Northwest (Goldenson et al. 2018).

Guan et al. (2013) also reported that the high frequency of ARs over California is favored by the negative phase of Arctic Oscillation (AO) and Pacific-North American (PNA) teleconnection patterns. While the negative AO tends to bring more precipitation in California (Guan et al. 2013) and cause more extreme precipitation when combined with positive Southern Oscillation Index (SOI) (McCable-Glynn et al. 2016), positive AO was also shown to increase wintertime precipitation (Matsuo and Heki 2012). McCable-Glynn et al. (2016) also concluded that there is an unclear relationship between the SST-based ENSO

index and that there is a connection with the frequency of ARs and the Walker circulation. However, the authors did not provide enough explanation or evidence to back up their conclusion which could be done with further examination. Most recently, using a self-organizing map, Kim and Chiang (2021) separated the various climate modes into two groups based on their synoptic variabilities, such as ENSO mode and jet mode (including AO index), and showed these synoptic patterns are closely associated with the distinct AR characteristics such as genesis, landfall location, and duration. However, this study also heavily relies on the reanalysis product, and the use of satellite or in-situ data over a long period of record is limited.

Figure 2 shows the example of precipitation of January 2009 and 2010 corresponding to negative and positive AO index, along with the time series of Global Precipitation Measurement (GPM) precipitation anomaly from the climatological mean (1980-2020) overlaid by AO monthly index. Although there is large month-to-month variability in precipitation and the impact of AO on the regional-scale precipitation can be limited due to the difference in temporal and spatial scales, we do see some noteworthy areas indicating possibly linkage between precipitation and AO. For example, high precipitation is observed over the northeastern Pacific and north of the western U.S. in January 2009, while high precipitation rate is found in the lower latitude such as Washington, Oregon, and northern California in January 2010, when AO is in opposite phase. Furthermore, for the higher precipitation events during 2003, 2006, 2010, and 2016, the AO index tends to have negative phase. In contrast, for the lesser precipitation events during 2007, 2012, 2014, and

2015, AO index tends to be high positive or marginally positive. Thus, how the different phase of the large-scale AO patterns impacts the characteristics of local precipitation over the western U.S., what synoptic conditions are shaped by the different phase of AO, and how they are related to SWE trends over the mountain region is worth to further investigate.

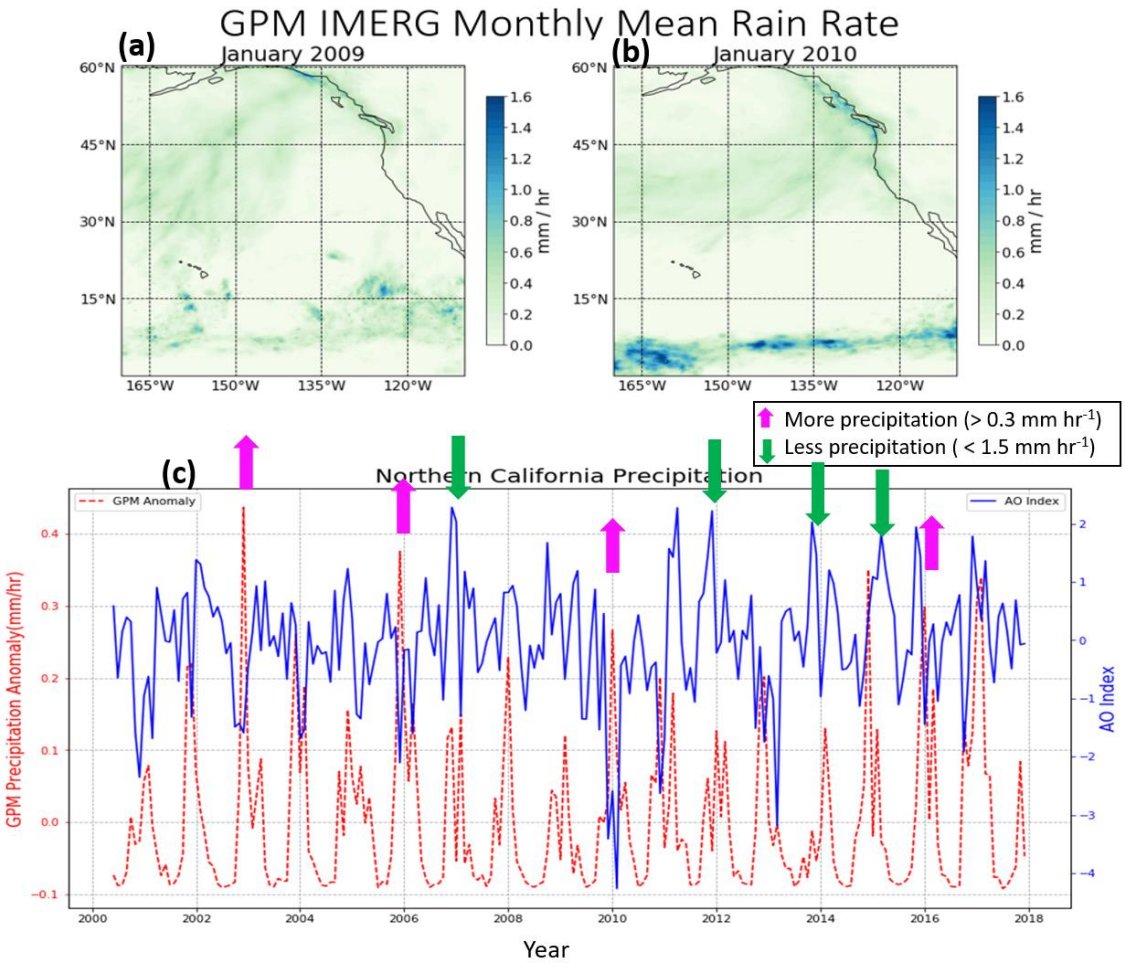

Fig. 2. Precipitation during (a) January 2009 and (b) January 2010. (a) and (b) corresponds to positive AO month and negative AO month, respectively. (c) Time series of monthly GPM precipitation and AO index. Precipitation data was calculated by taking the average over the entire northern CA area. Decreases of precipitation highlighted in green and increases in yellow. The northern California is averaged over 122 -124 °W and 36.5 -42°N.

In this study, we use about 40 years of NASA MERRA2 reanalysis data combined with the IMERG satellite data to extensively investigate the relationship of the different phases of AO, and how they are coupled to the synoptic conditions that favor ARs. For the case study, the surface-based observation snowpack, surface temperature, and precipitation data will also be utilized to link them to AO phases. We will describe the data and methods in section 2. The dominant synoptic patterns during the different phase of AO and associated AR characteristics will be examined in section 3. The case study of rain on snow events during three different phases of AO months will be also presented. In section 4, the discussion and conclusions of this study will be shown.

2. Data and methods

2.1. Data

2.1.1. MERRA2

Several of the variables analyzed in this study were collected from NASA's Modern-Era Retrospective analysis for Research and Applications version 2 (MERRA2) including sea level pressure (SLP), geopotential height at 1000 hPa and 500 hPa, air temperature at 850 hPa, horizontal wind (u, v) at 850, 500, and 250 hPa, vertically integrated water vapor flux and potential temperature. Both instantaneous 3-dimensional and time-averaged 2-dimensional mean monthly data collections were implemented with spatial resolution of 0.5° x 0.625°. Produced by the Global Modeling and Assimilation Office (GMAO) of NASA, MERRA2 uses the Goddard Earth Observing System Model (GEOS) version 5.12.4 and covers the time period of 1980 and onward.

The integrated water vapor transport (IVT), calculated in kilograms per meter per second, is a key factor in determining atmospheric rivers' strength and precipitation outcome (Ralph et al. 2019). Additionally, we use IVT as a proxy for precipitation in the area we are studying. The IVT data was initially measured from the MERRA2 reanalysis product and then collated into an AR catalogue by Jonathan Rutz from the University of Utah. IVT was calculated using the following formula:

$$IVT = \frac{1}{g}\int_{p_{sfc}}^{100\ hPa} q\boldsymbol{V}\ dp\ , \qquad (1)$$

where p_{sfc} is the pressure at the surface, q is the specific humidity, $\boldsymbol{V}$ is the total wind vector, and g is the gravitational acceleration (Rutz et al. 2014). We collected IVT data from three sites spanning the six different regions to get a large-scale average. This was important to do since the AO index is a global climate fluctuation and would likely only have impact on larger regional areas. The data was originally computed at a three hourly timescale and later averaged into monthly data for time series analysis. Additional data used from this database were AR duration in 3-hour time resolution and new AR summation.

2.1.2. GPM

Precipitation data were acquired from NASA's Integrated Multi-satellite Retrievals for GPM (IMERG) project with daily and monthly resolution. This data were collected from its inception in 2000 through to 2020 and were in a monthly timescale resolution. In Fig. 2c the monthly anomalies were calculated for this data to remove the seasonal mean features and plotted on a timescale series.

2.1.3. Arctic oscillation (AO) and climate indices

The Arctic Oscillation (AO) index is a measurement of geopotential height anomalies north of 20° N (National Centers for Environmental Information 2021). This data were collected from the National Weather Service's Climate Prediction Center. The index is measured daily and was collected as a monthly average which has a lot of variability when examining a forty-year period and so to smooth out some of that variability we calculated the three-month running average (Figs. 17, 18, 22). Since climate conditions are at their

most variable during winter months and AO is a measure of conditions in regard to the Arctic region, it then follows that the most affected months are December through March.

2.1.4. Snow water equivalent (SWE) and precipitation

Data used to analyze snow accumulation and corresponding total precipitation were gathered from the California Data Exchange Center provided by the California Department of Water Resources (2021). Since this database mainly covers the state of California, time and spatial aspects of our data were limited by this. In addition, since the quality of the reanalysis data in the mountain or near-surface regions is poor or unavailable (Scherrer 2020), surrounding air temperature measurements were used in this SWE analysis and collected from the same local sites. These in-situ measurements consisted of a network of snow sensors used to calculate the snow water content and rain gauges for the total precipitation for the case study. We also used these measurements to determine rain-on-snow (ROS) events which were anytime where the snow water equivalent (SWE) decreased while the total precipitation increased.

2.2. Methodology

The behavior of ARs varies greatly based on locations (Harris et al. 2018). In this study, we separated the whole western United States coastal region into six subregions: A) Washington/Oregon coast, B) Northern California coast, C) Northern California inland, D) California Mountains, E) Southern California coast, and F) Southern California Inland. We calculated the percentage difference seen in Figs. 13-15 by subtracting the total months

(1980-2019) average from the total average of positive or negative AO months (Tables 1 and 2) and dividing by the total months average.

To determine the correlation of IVT and precipitation we calculated the coefficient of correlation (R^2) and the Pearson correlation coefficient (R). In Figs. 3 and 5, to account for seasonal and monthly variations and get a better understanding of how each month was different than the 40-year climatological mean of 1980 through 2019, we calculated the anomaly for each analyzed month for SLP and geopotential height at 500 hPa respectively. The formula for used to calculate these anomalies was as follows:

$$A\% = \frac{(m_a - c_a) \times 100}{c_a}, \qquad (2)$$

where m_a is the average of the analyzed month and c_a is the climatological mean of that month. We also calculated the anomaly of the variables only for positive AO months and negative AO months. For those analyses we calculated the average for all AO months greater than 1.5 or less than -1.5 for the positive AO phase and the negative AO phase respectively.

3. Results

3.1. Synoptic characteristics of ARs in different phases of AO

3.1.1. Sea level pressure

Charting the AO phase from all the months greater than 1.5 and less than -1.5 from 1980 to 2019 gives us Tables 1 and 2. From this we found the top positive AO and top negative AO months from these 40 years. We then compared the top two positive and negative AO months to the whole 40-year span. Since synoptic conditions can be affected by the different phases of climate modes, examining these conditions are an important first step. Figure 3 shows the distinct SLP patterns in the different phase of AO from the top two positive and negative AO months. Although there is substantial month-to-month variability, the positive phase tends to have high pressure systems centered in the northeastern Pacific off the coast of Alaska with lower-than-average sea level pressure over the Arctic. Negative AO months tend to show the opposite pattern with low pressure systems centered in the eastern Pacific Ocean and higher than average pressure in the Arctic region. These patterns may prevent cold Arctic flow from moving southward in the positive AO months compared to negative AO months.

Table 1. Positive AO months from 1980-2019 greater than 1.5 in decreasing value of AO index value

Month-Year	AO Value	Month-Year	AO Value
Jan-93	3.495	Feb-97	1.889
Feb-90	3.402	Mar-94	1.881
Feb-89	3.279	Apr-90	1.879
Jan-89	3.106	Mar-15	1.837
Mar-90	2.99	Dec-16	1.786
Dec-06	2.282	Nov-94	1.779
Apr-11	2.275	Dec-88	1.679
Dec-11	2.221	Oct-08	1.676
Mar-19	2.116	Dec-92	1.627
Jan-07	2.034	Dec-91	1.613
Nov-13	2.029	Jun-94	1.606
Nov-15	1.945	Feb-11	1.575
Mar-86	1.931	Mar-89	1.53

Table 2. Negative AO months from 1980-2019 less than -1.5 in increasing value of AO index value

Month-Year	AO Value	Month-Year	AO Value	Month-Year	AO Value
Feb-10	-4.266	Jan-80	-2.066	Mar-06	-1.604
Dec-09	-3.413	Dec-85	-1.948	Dec-02	-1.592
Mar-13	-3.185	Oct-16	-1.917	Nov-00	-1.581
Feb-86	-2.904	Feb-83	-1.806	Oct-09	-1.54
Jan-85	-2.806	Dec-12	-1.749	Feb-04	-1.528
Dec-10	-2.631	Mar-87	-1.746	Apr-96	-1.525
Jan-10	-2.587	Dec-96	-1.721	Oct-12	-1.514
Mar-84	-2.386	Mar-01	-1.687		
Dec-00	-2.354	Jan-04	-1.686		
Dec-95	-2.127	Jan-11	-1.683		
Dec-05	-2.104	Mar-81	-1.645		
Jan-98	-2.081	May-93	-1.607		

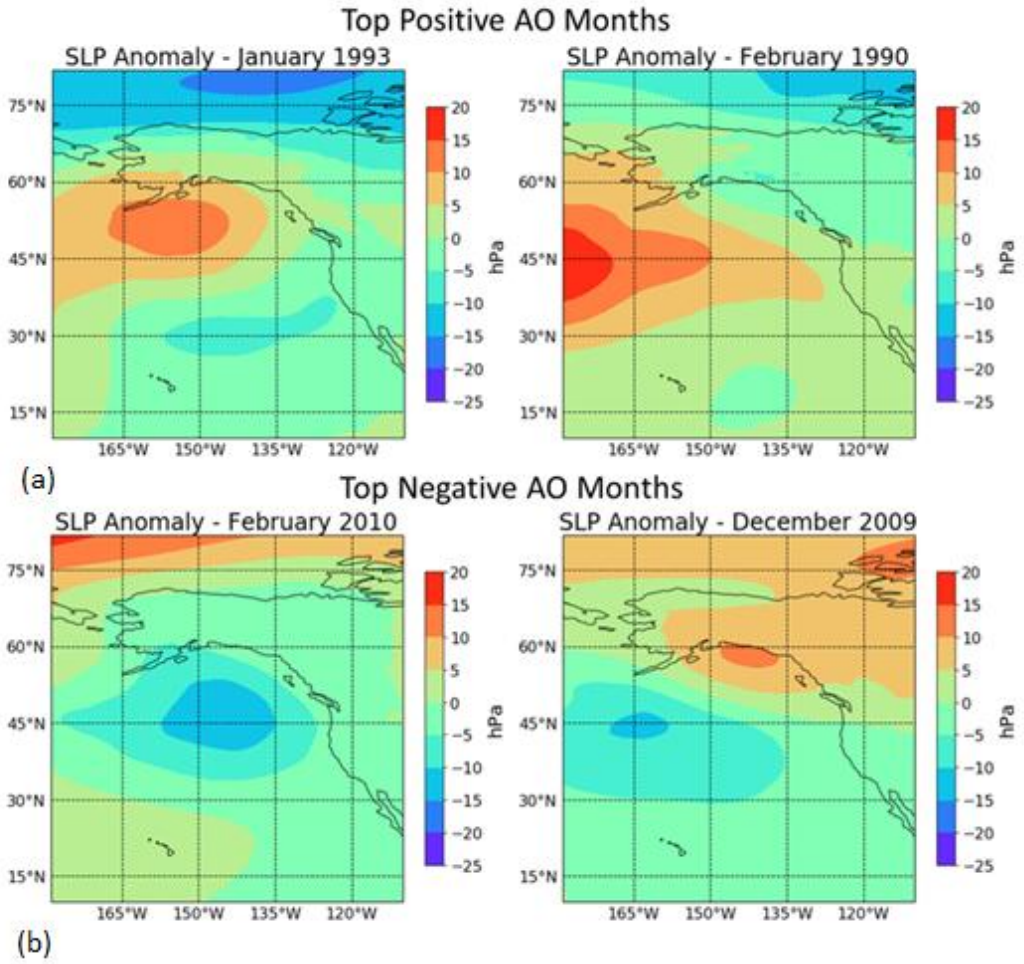

Fig. 3. Longitude-latitude cross section of SLP anomaly for the top two (a) positive AO months and (b) negative AO months.

Examining the average SLP for all positive AO months and all negative AO months greater than 1.5 or less than -1.5 respectively is shown in Fig. 4. This average of major negative AO months (Fig. 3b) confirms the SLP pattern seen in the top two negative AO months, lower pressures off the coast of Alaska and high pressure in the Arctic. For the average of positive AO months (Fig. 4a) a similar pattern is also present, however both the low- and high-pressure systems are farther south than what is seen in the top two AO months. The two things of note from this figure are seen in the negative AO months plot

which has a lower low-pressure system in the northeast Pacific and a much higher high-pressure system in the Arctic as compared to the positive AO months. This confirms the pattern shown in the SLP differences during AO phases (Thompson and Wallace 1998) shown in Fig. 3. It also indicates there can be more meridional flow developing associated with the low-pressure system during the negative phase.

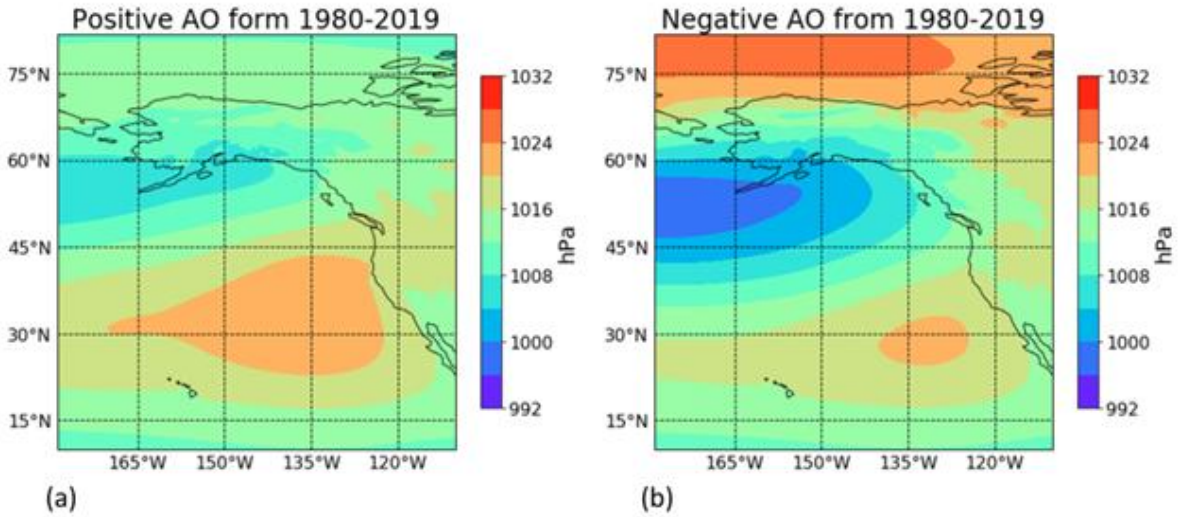

Fig. 4. Composite SLP anomaly of all positive AO months greater than 1.5 (a) and all negative AO months less than -1.5 (b) compared to all months from 1980-2019.

3.1.2. Geopotential height and air temperature

We did the same process with geopotential height as with SLP, taking the top two positive and negative AO months and inspecting them for consistencies. The geopotential height at 500 hPa had similar patterns to the 850 hPa and 250 hPa (not shown) so only 500 hPa geopotential height was used and is demonstrated in Fig. 5. The geopotential height anomaly patterns are also very similar to those seen in the sea level pressure field (Fig. 3). We can therefore use this similarity to confirm our assumptions from the SLP map. The

positive difference of height anomalies between the extratropical region and the Arctic region seen in the positive phase of AO (Fig. 5a) would limit north-south meridional flow while the negative difference seen in the negative phase (Fig. 5b) proposes a prospect for more north to south flow of air.

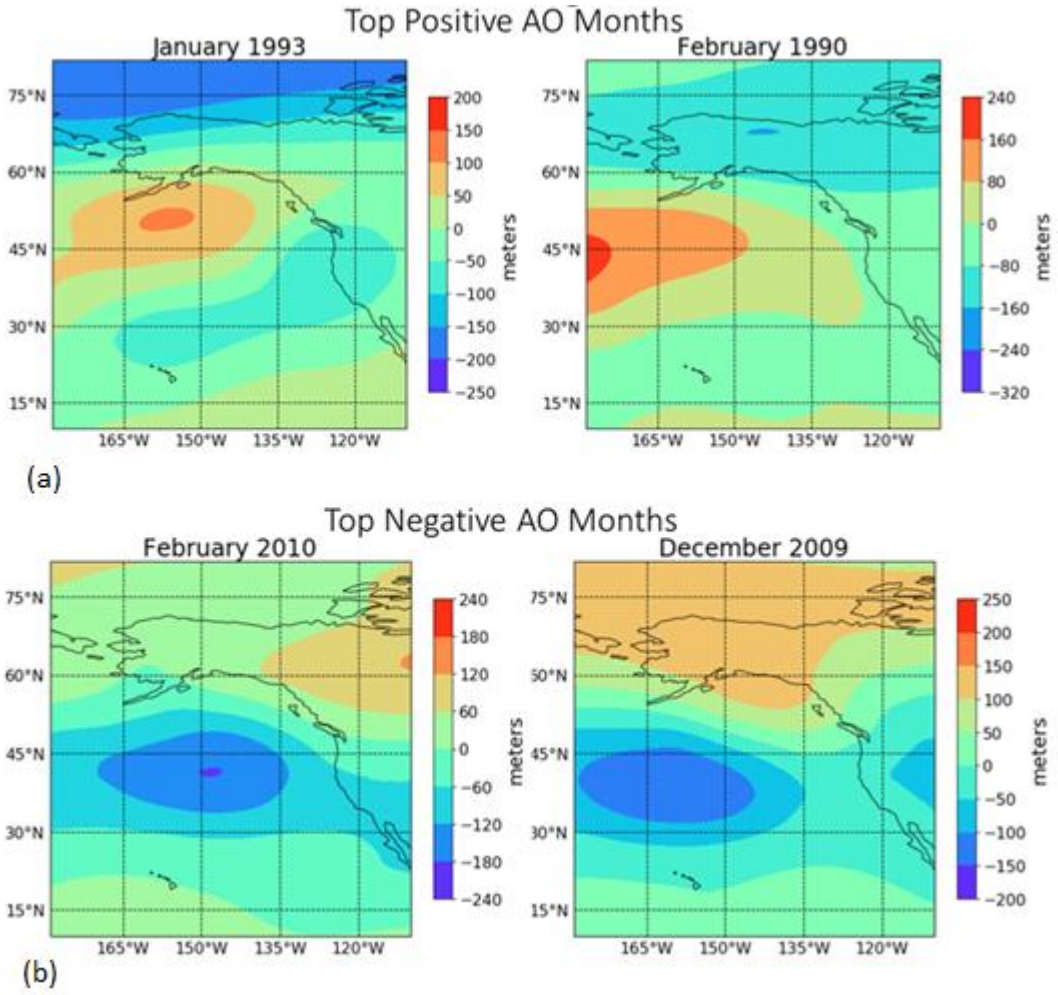

Fig. 5. Longitude-latitude cross section of geopotential height at 500 hPa anomaly for the top two (a) positive AO months and (b) negative AO months.

The composite plots for geopotential height anomaly for the positive phase and negative phase of AO are shown in Fig. 6, respectively. In the negative AO months (Fig. 6b)

we see low pressures in the eastern Pacific southwest of Alaska as was in Fig. 4, albeit a bit farther south. However, the positive AO months (Fig. 6a) do not have the same high-pressure system in the pacific as seen in the SLP map. The positive AO months do differ from the negative AO months in that higher pressures, although still negative pressure anomalies, extend higher in latitude and lower pressures are consistent over the Arctic region. Additionally, there is still the same extratropic to Arctic region pressure difference that was visible in all previous figures which further suggests more northerly flow and therefore more wavelike patterns during negative AO months and less during positive AO months.

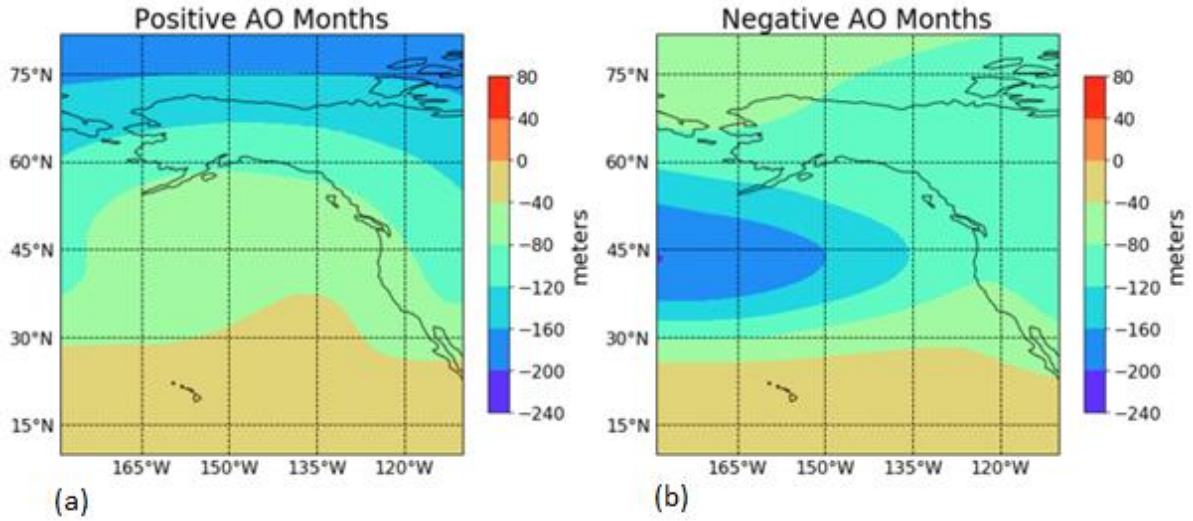

Fig. 6. Composite mean geopotential height anomaly at 500 hPa of all positive AO months greater than 1.5 (a) and all negative AO months less than -1.5 (b) compared to all months from 1980-2019.

The MERRA2 air temperature anomaly at 850 hPa averaged for positive and negative AO months as done in Figs. 4 and 6 is shown in Fig. 7. Seen in this plot are some mirrored patterns with the 500 hPa geopotential field, especially the colder temperatures over the

extratropical Pacific region in the negative AO months where the low pressure in Fig. 6 is also located. Warm temperatures extend northward in the Eastern Pacific in positive AO months but more so in negative AO months. This tends to provide favorable conditions where the negative AO months have a higher meridional temperature gradient than in the positive phase and which in turn would be an indicator of possibly stronger vertical wind shear in the region of the eastern Pacific where much of western U.S. landfalling ARs originate.

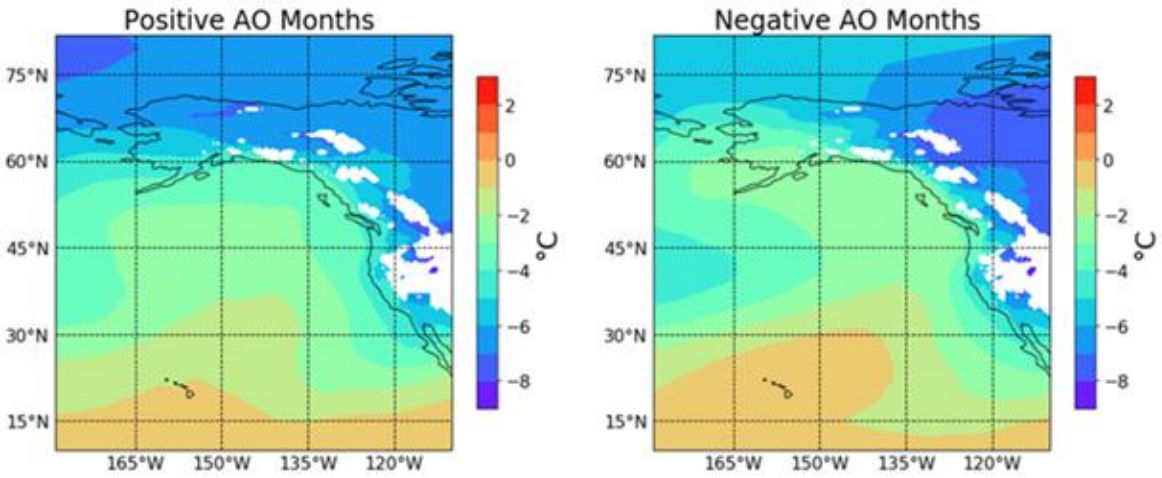

Fig. 7. Average temperature anomaly at 850 hPa of all positive AO months greater than 1.5 and all negative AO months less than -1.5 compared to all months from 1980-2019.

3.1.3. Wind speed and water vapor flux

Next, we looked at horizontal wind speed for the positive and negative AO months. Breaking down the wind speed into its components and averaging all top positive and negative AO months for the 850 hPa, the 500 hPa and 250 hPa levels, we get Figs. 8 and 9. The zonal wind maps show that in the negative AO phase, there are strong areas of easterly and westerly winds in the 35° N and 60° N regions at all three levels that are closer to the

North American coast than in the positive AO months (Fig. 8c). Here we see opposing patterns in the positive phase and the negative phase of AO where there is an area band to the west of the California coast that has lower wind speeds during the positive phase and higher wind speeds during the negative phase (Fig. 8c). We also found that the low-level jet, defined as high wind speed at around 1 km and plays a critical role to transport moisture during ARs, occurs more favorably during negative AO phases (Fig. 8c, right). This indicates conditions in negative AO phases may provide the favorable conditions to more intense AR over the western U.S., consistent with the result by Guan et al. (2013). Examining the 500 hPa and 250 hPa levels (Fig. 8a, b) we also see a stronger upper-level jet which also has influence on low-level, and therefore AR, moisture transport (Brill et al. 1985). In all three levels of the negative phase in the 45° to 60° N range, there are also strong positive meridional winds. This can be an indicator of greater wavelike air movement during the negative AO phase and is confirmed when examining the upper level (250 hPa) geopotential height contours and wind vectors (Fig. 10). Here we also see the lesser wavelike pattern in the positive AO months. From Figs. 8 and 9, we can see a greater eastward air movement in the region that is highly associated with landfalling ARs in the United States west coast. Additionally, we see in the positive months more ridge-like patterns that could block the formation of extratropical cyclones and more trough-like patterns in the negative AO months which can carry northward tropical moisture that fuels atmospheric rivers.

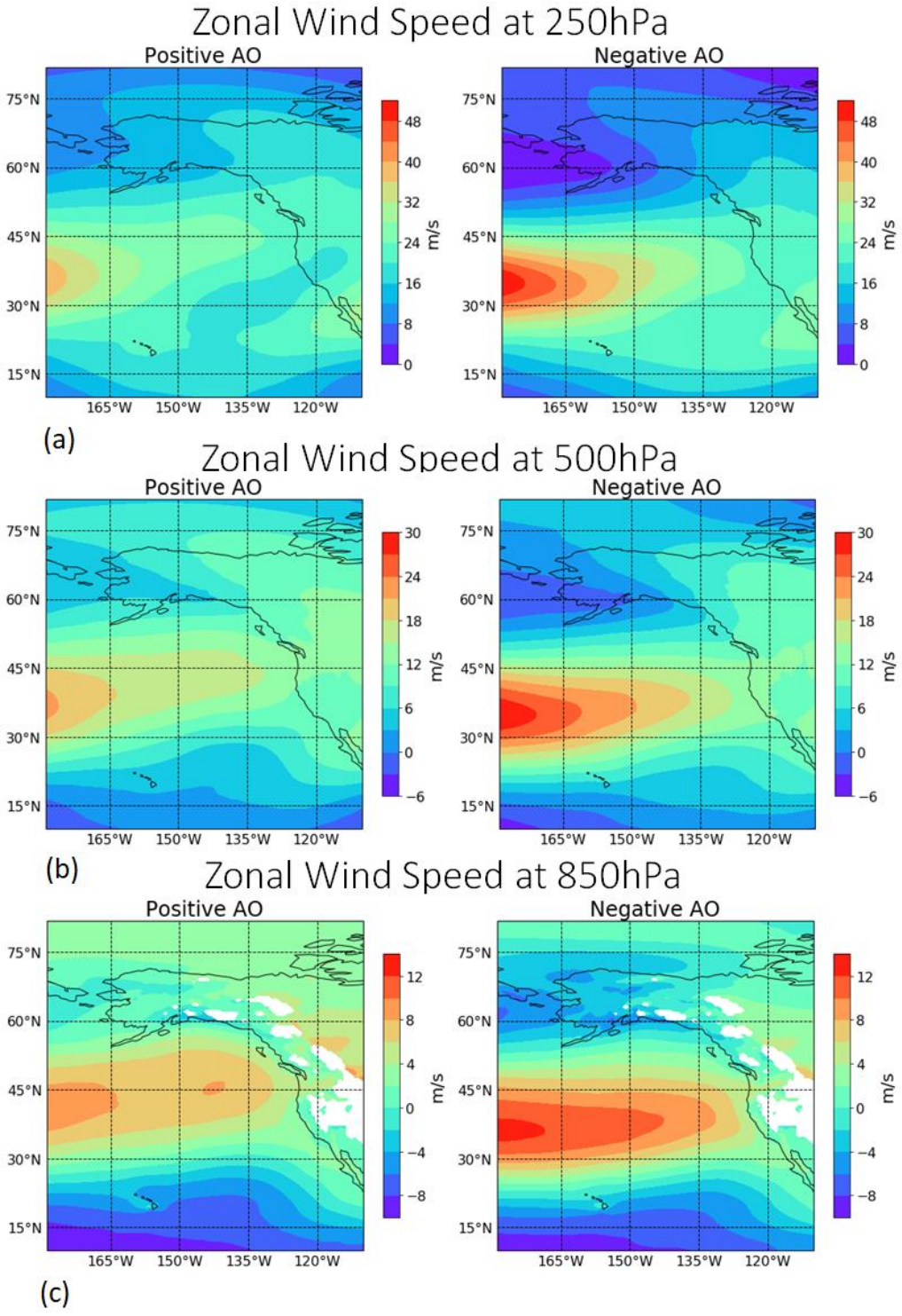

Fig. 8. Composites of zonal wind speed of all positive AO months greater than 1.5 and all negative AO months less than -1.5 for 250 hPa(a), 500 hPa(b) and 850 hPa(c) levels.

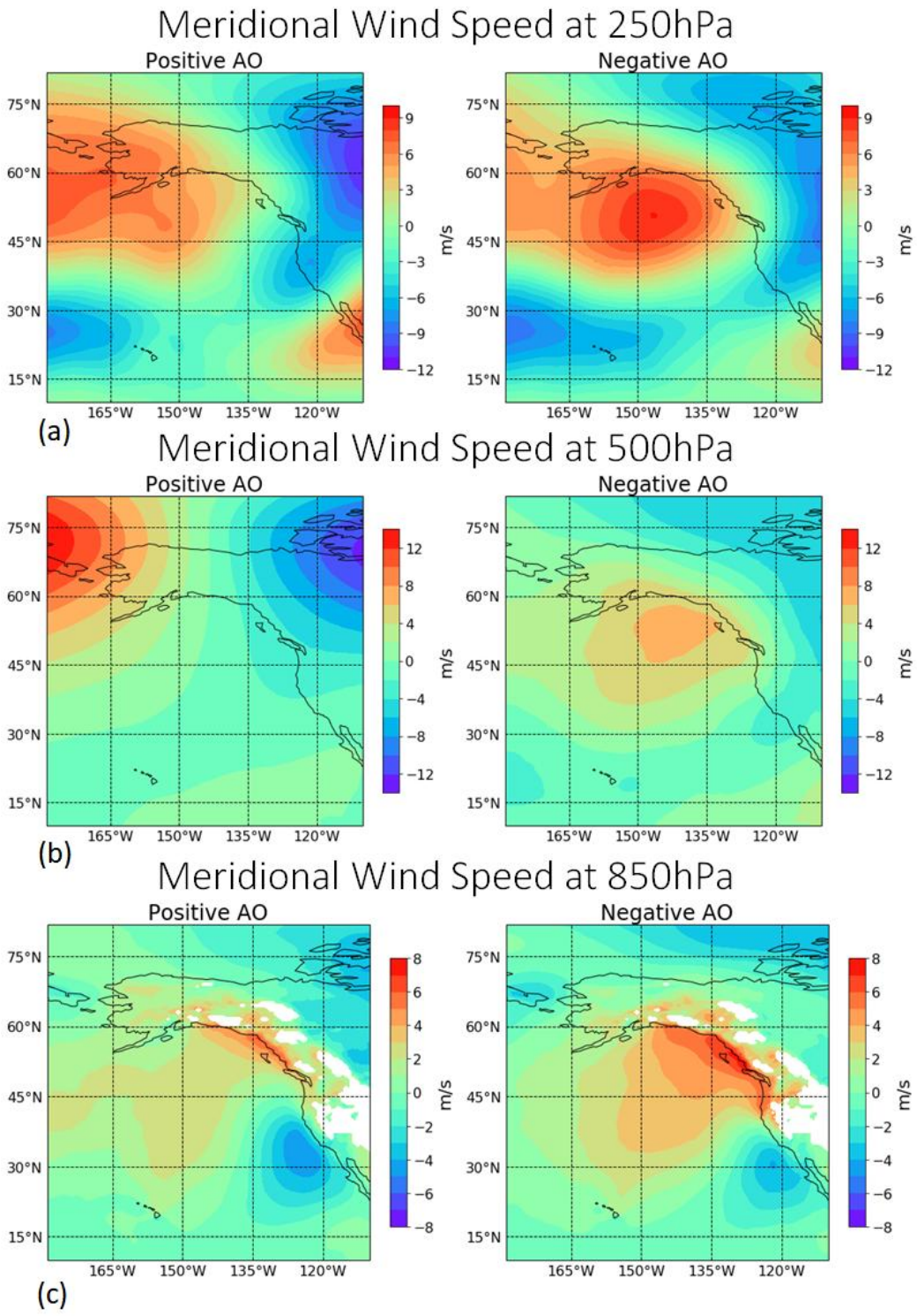

Fig. 9. Composites of meridional wind speed of all positive AO months greater than 1.5 and all negative AO months less than -1.5 for 250 hPa(a), 500 hPa(b) and 850 hPa(c) levels.

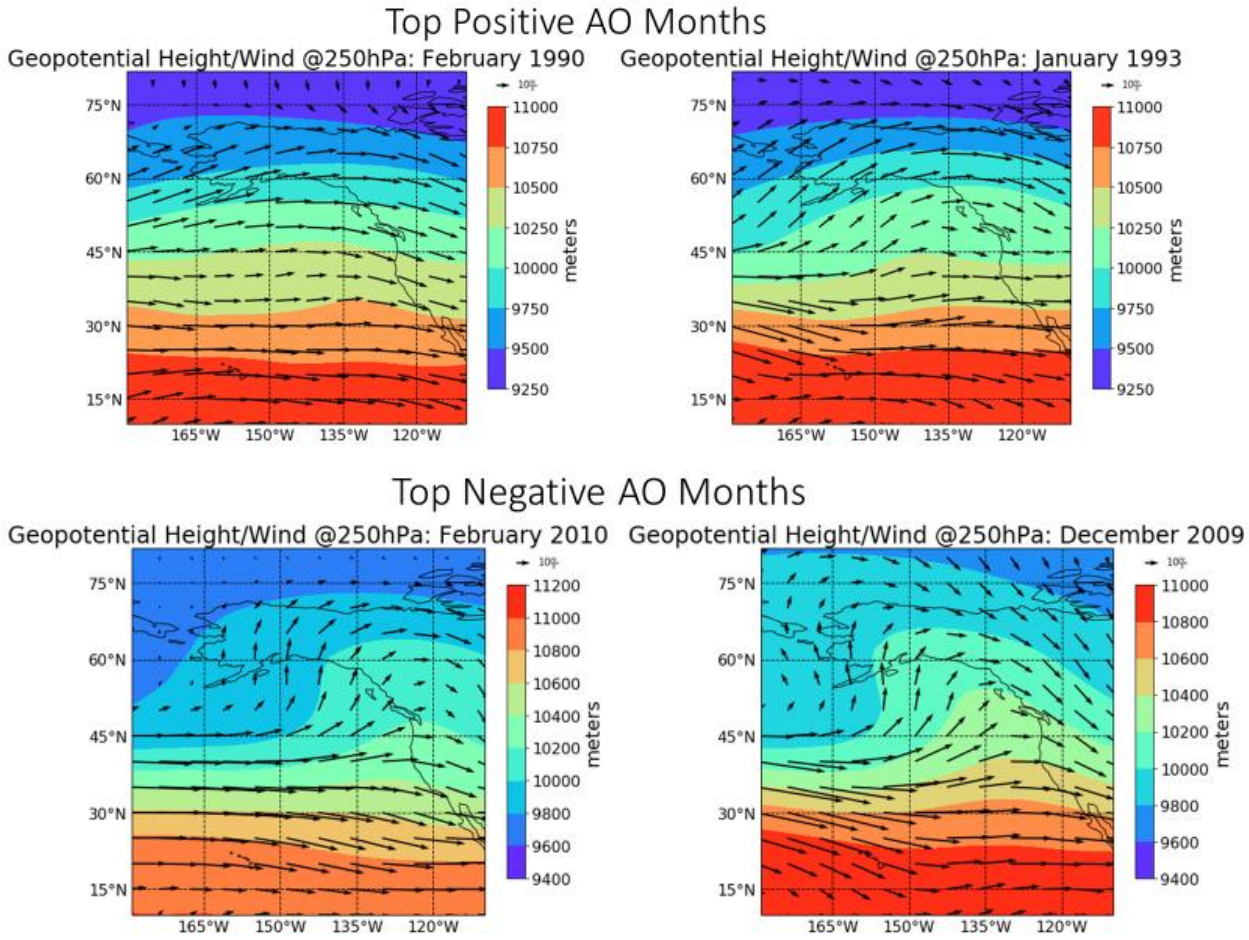

Fig. 10. Longitude-latitude cross section of geopotential height and wind vectors at 250 hPa for the top 2 positive AO months (top) and the top two negative AO months (bottom) from 1980 to 2019.

Together with the wind speed and winds at different vertical levels, we also examine the average zonal, vertically integrated water vapor flux during the positive and negative phases of AO, shown in Fig. 11. Here we see a remarkable increase in west to east vapor flux in the negative AO months over the positive AO months. Figure 11, along with the previous wind plots, suggests that the synoptic conditions indispensable for AR formation, such as strong

low-level jet with high moisture and strong vapor flux, is well formed during the negative phase of AO over the northwestern U.S. in northern hemisphere wintertime.

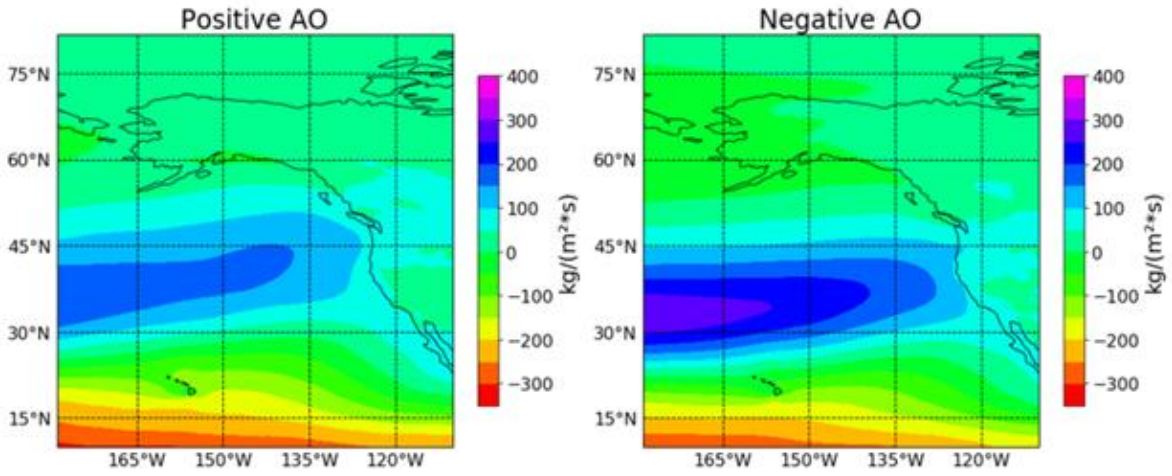

Fig. 11. Composite of the monthly zonal water vapor flux of all positive AO months greater than 1.5 and all negative AO months less than -1.5.

3.2. Different AR characteristics during the different phases of AO

3.2.1. AR intensity, duration, and frequency

To examine how the different phases of AO are related to AR characteristic such as intensity, duration, and frequency in local scales, we analyzed different regions over the West Coast of the United States, shown in Fig. 12(left). In this analysis we employed Jonathan Rutz's AR data catalog (Rutz et al. 2014) to observe any differences between positive and negative AO months compared to all months in the time span of 40 years (1980–2019). The six sub-regions were chosen from across the western United States to observe any differences between the regions. Three locations were then picked from the top, middle and bottom of each sub-region for a total of 18 locations and datapoints.

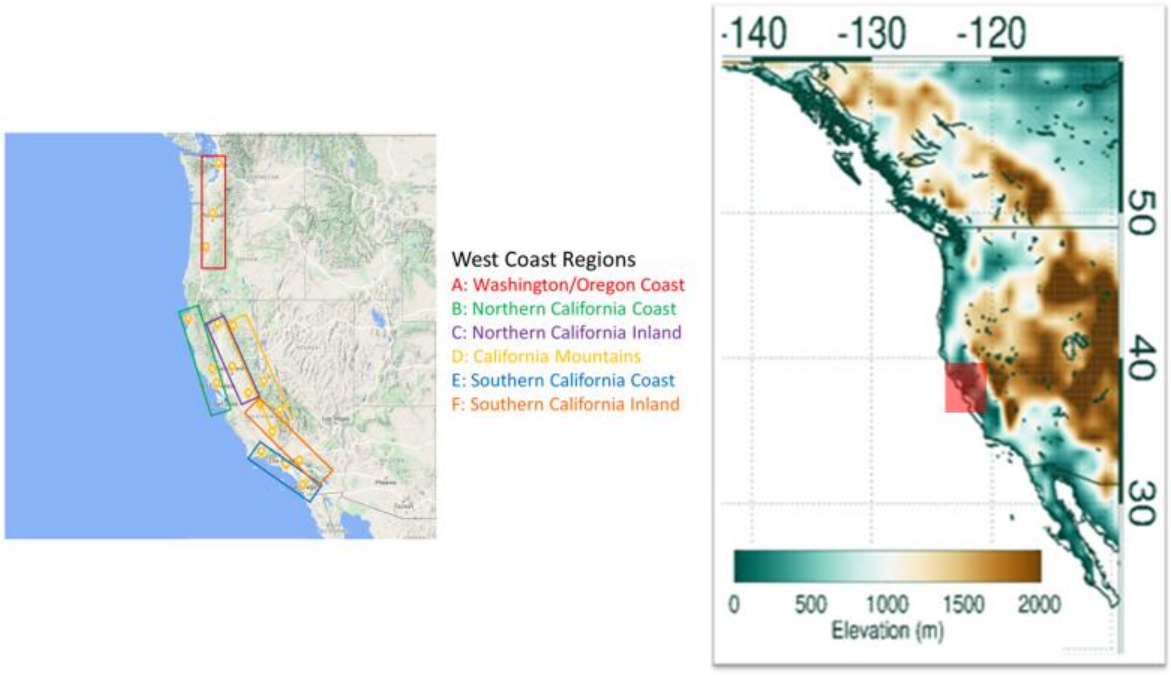

Fig. 12. (Left) Map of studied regions in Fig. 12 created on Google Maps©. (Right) Map showing terrain elevation showing studied area for Figs. 16-18.

The IVT is averaged for all AR events (when the IVT was greater than 250 kg/m/s) during all of the positive AO months during the 40-year period and we found the percentage difference from all AR events in that same time period shown in Fig. 13a. Similar method is applied to data for all negative AO months in Fig. 13b. Notably, the AR IVT is lower during the positive phase of AO and higher during the negative phase months for almost all regions. Taking the averages for all 18 sites yields a difference of -2.81% and 5.39% for the

positive and negative AO months, respectively.

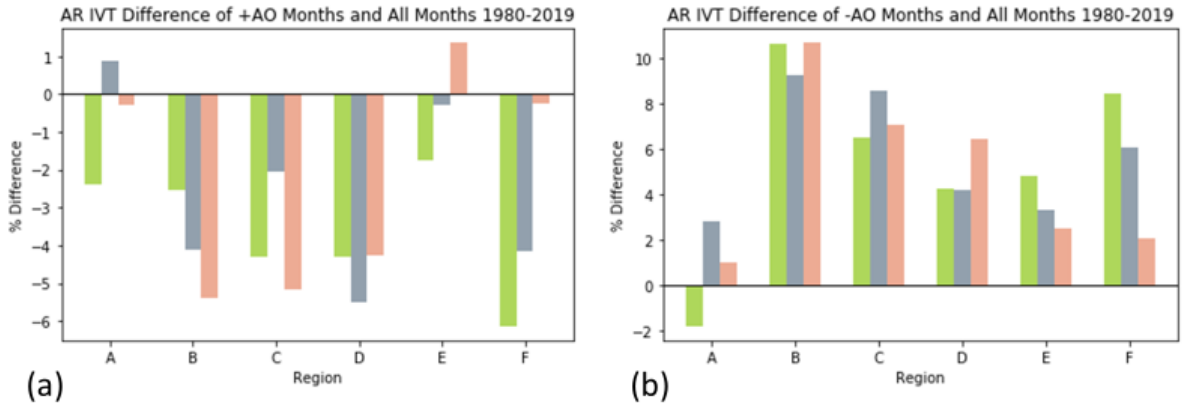

Fig. 13. Percentage difference histograms of IVT for regions referred to in Fig. 3 during positive AO months and negative AO months represented by regions shown on map shown in Fig. 12.

Figure 14 shows the duration difference of each new AR event during the different phase of AO quantified in hours. Also like the AR intensity plots (Fig. 13), there is a characteristic feature: shorter durations compared to all months during the positive phase of AO and longer durations during the negative phase in most of the locations. The overall mean difference for each of these phases is -19.96% for the positive phase and 22.02% for the negative phase.

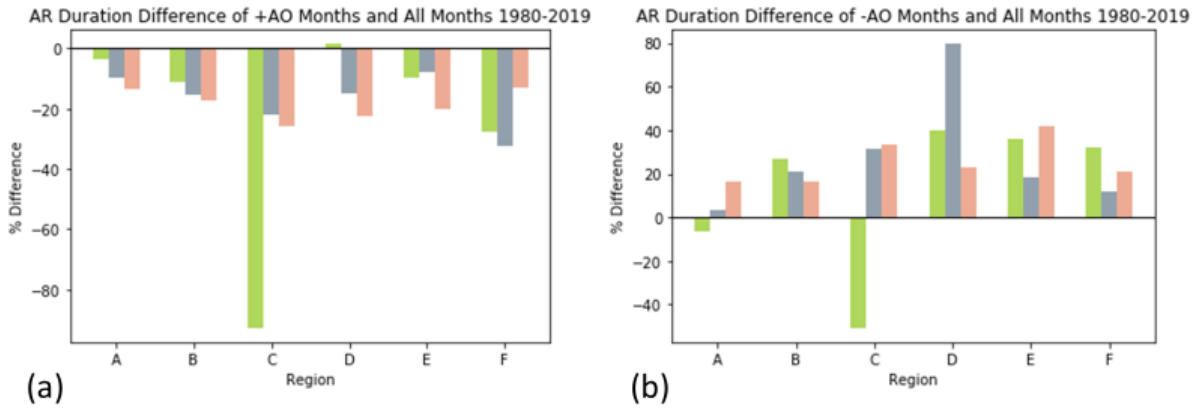

Fig. 14. Percentage difference histograms of AR duration in hours for regions referred to in Fig. 3 during positive AO months and negative AO months represented by regions shown on map shown in Fig. 12.

The AR frequency difference in the two phases of AO is also analyzed and compared, as shown in Fig. 15. It is found that the percentage difference of ARs per month for positive and negative AO months in comparison to all months also showed an overall negative difference during positive AO months with a total average of -2.64% and a positive difference during negative AO months with a total average of 44.7% (Fig. 15). Given the three characteristics for the severity of atmospheric rivers shown in Figs. 13 – 15, negative AO months favor AR formation, intensity, and longevity, compared to the positive AO months over most of the coastal and mountainous regions of California.

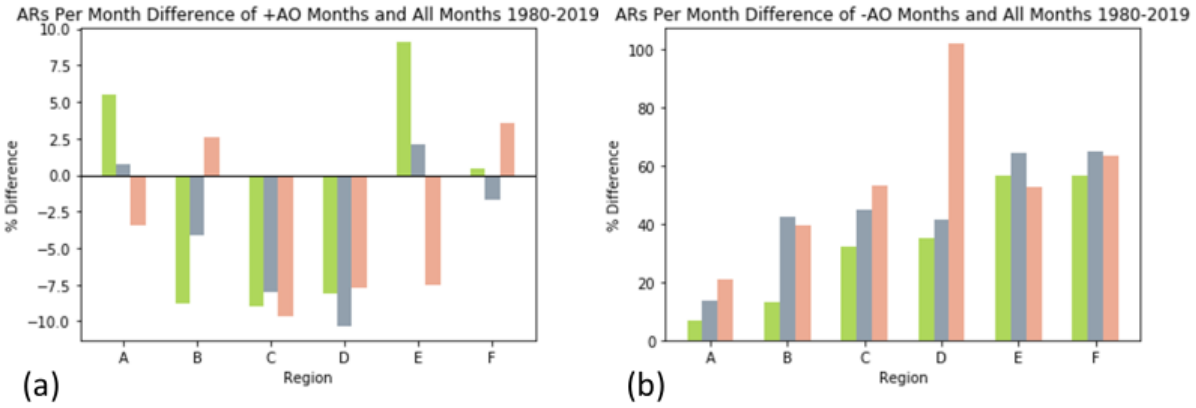

Fig. 15. Percentage difference histograms of AR frequency per month for regions referred to in Fig. 3 during positive AO months and negative AO months represented by regions shown on map shown in Fig. 12.

3.2.2. IVT and AR intensity

In Fig. 2, we see higher rain rates are found farther north in the positive AO phase compared to the negative phase (Figs. 2 (a, b)). As for the negative AO month, we see higher rain rates and precipitation on land at lower latitudes.

With that established, we then examined the AO Index compared to precipitation over a larger time period, 1980 to 2019, to find any possible trends or if the relations from the shorter time span held up. Since the GPM satellite data began in 2000, another data source had to be used so here we used integrated water vapor transport (IVT). In Fig. 16 we see that we have a good correlation between IVT and precipitation (R^2 value of 0.645) for Northern California. From this we can confirm that IVT can be used as a proxy for precipitation assumptions. From Fig. 17 we see some similar associations between the IVT, and the AO Index shown in Fig. 2. In the green shaded areas, there are increases in the IVT (red line) while there are decreases in the AO index (blue line) and in the yellow areas we

see drops in IVT with spikes in the AO index. The same for Fig. 17 can also be determined for Fig. 2b, though some connections are present there is mostly large amounts of variability so other factors must influence ARs during positive and negative AO months.

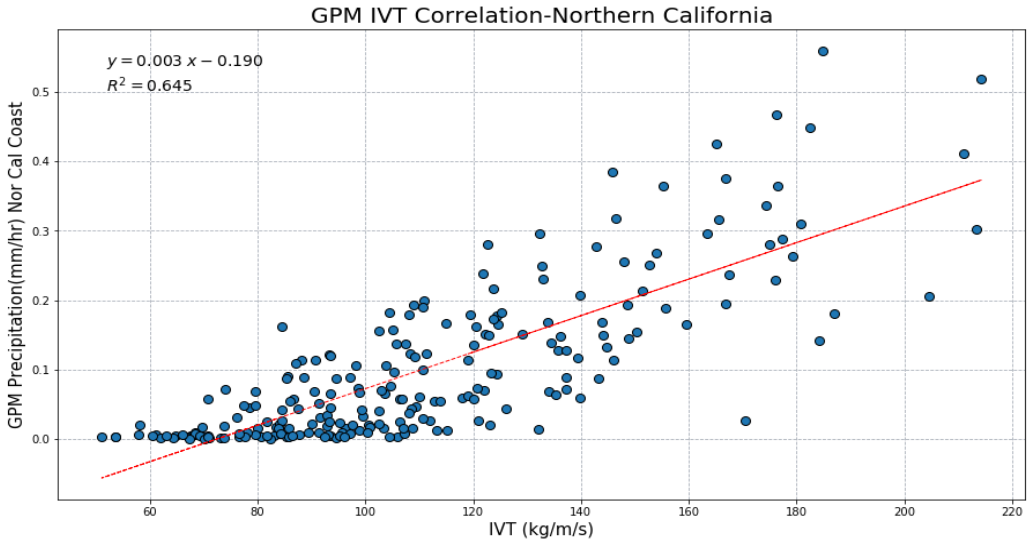

Fig. 16. Scatter plot of monthly averaged IVT and GPM precipitation over Northern California (shown in red in Fig. 11, left and averaged over whole area for 2000-2019

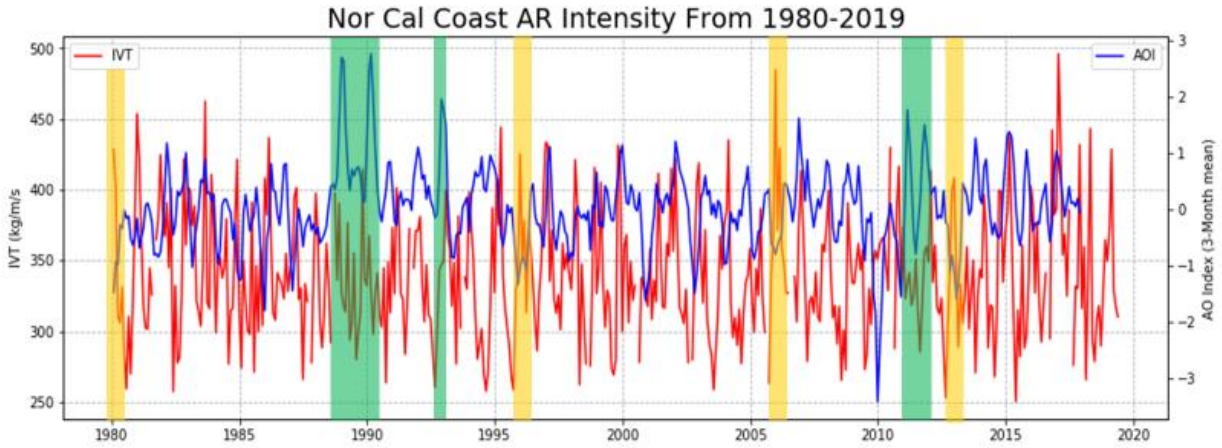

Fig. 17. Time series of IVT and three-month averaged AO index and the analyzed area highlighted in red on the elevation map on the right. IVT calculated by averaging three points spread over the northern CA coast area. Decreases of IVT highlighted in green and increases in yellow.

3.3. SWE characteristics over the northern California during the different phases of AO.

3.3.1. SWE and ROS events in relation to AO

We then examined how AO could modulate regional snowpack through snow water equivalent (SWE) measurements. Figure 18 displays the time series between SWE, AO index and the temperature at 850 hPa. For the SWE time series seen in both plots of Fig. 18, we calculated the monthly anomaly to extract the anomalous features at the given year compared to the climatological mean. In this time span from 1984 to 2020 we see a few instances of reduced snow water equivalent and both higher temperatures and higher AO index. For example, during 2015-2016, very low SWE anomaly is observed when temperatures warmer than the climatological mean are simultaneously observed. Sea surface temperature (SST) is also reported to be very high, marking them as weak/strong El Niño, indicating the possible influence of the El Niño event on AR precipitation during this period (Zechiel and Chiao 2021). Out of all the months from 1984 to 2020, the positive AO months greater than 1.5 had 71.4% negative SWE anomalies, as compared to all months with 63.7% negative SWE anomalies, and negative AO months less than -1.5 with 33.3% negative SWE anomalies (Fig. 18). This suggested connection led to our next case study involving rain-on-snow (ROS) events, air temperature, and AO index. Here we compared a few ROS and SWE events by separating them within 3 different AO types: 1) a high positive AO month 2) an AO month with a value close to 0, and 3) a high negative AO month from four different locations in the mountainous regions of Northern and Central California, indicated on Fig. 19 and Table 3. We also computed for each month the total monthly

precipitation, the average daily ground air temperature, the monthly average temperature, the total increase and decrease of SWE and the ratio of snow accumulation to total precipitation, summarized in Table 3.

When comparing the number of ROS events, we see that there are more ROS occurrences during the positive AO month 50 % of the time (two out of the four locations; Guan et al. 2016), one instance of more ROS during a negative AO month, and one instance of no ROS during either month. From this we cannot make any definitive conclusions about ROS events and AO. Additionally, in all four of the sites there was a higher monthly average temperature in the positive AO month. This indicates a possible connection between higher AO and higher average temperature. Over the entire time periods, we couldn't find any robust correlation between the entire time series of precipitation, temperature, and AO index (not shown), indicating that there may be other factors modulating these variables in different atmospheric conditions. Furthermore, the limited number of samples and the confined geological consideration due to the data availability in this study also hindered us to get to the full understanding of the factors controlling SWE during ARs over the western U.S.

We also did not pursue the detailed analysis for the relationship among AO-AR-SWE-ROS, because 1) the case studies using March 2016 and January 2017 data showed that there is almost the same or insignificant impact of AR and non-AR on ROS (~50%) as shown above, and 2) the limitation of SWE data makes the interpretation difficult. Instead, we focus on the further investigation of the association between SWE and AO during the

selected time periods and their linkages with the recent shifted climate patterns in the following section.

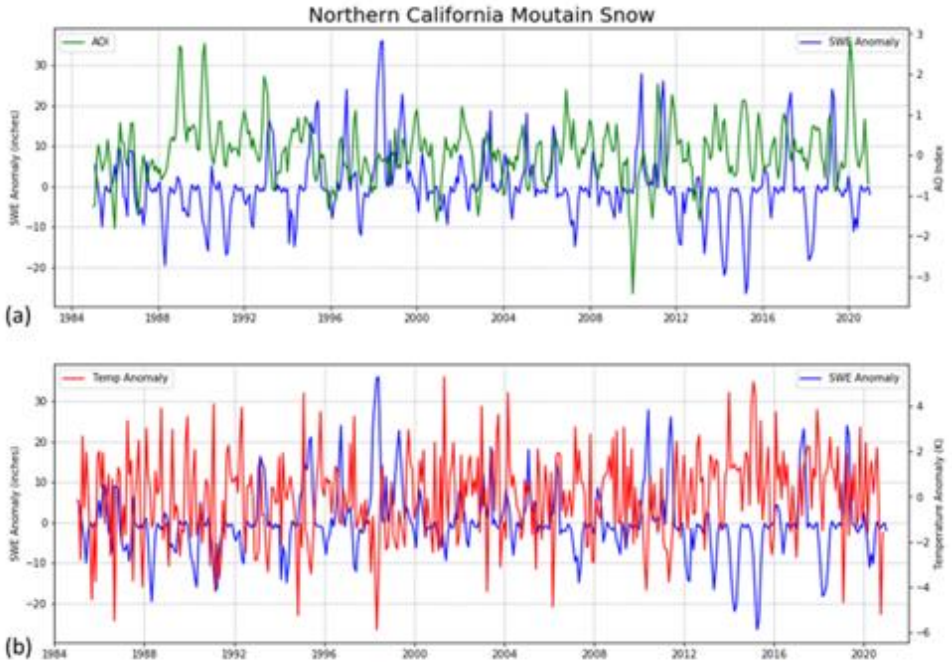

Fig. 18. Time series of snow water equivalent (SWE) anomaly for the Northern California Mountain region, an average of four different sites across the region, the 3-month average AO Index(a) and air temperature anomaly at 850 hPa(b) from 1984 to 2020.

Fig. 19. Map of northern and central California created on Google Maps© with the locations used for the SWE case study marked.

Table 3. Comparative chart of positive AO, neutral AO, and negative AO months for ROS events, average monthly ground temperature, total precipitation, SWE variations, and the ratio of SWE accumulation to total precipitation

Peterson Flat (41.30°N, -122.53°W)							
	AO Value	# of ROS	Avg. Temp. (°F)	Total Precip. (in)	SWE Increase (in)	SWE Decrease (in)	SWE Increase/ Total Precip.
Dec. 2006 (+AO)	2.28	3	33.42	3.48	13.08	9.12	3.76
Dec. 2018	0.11	1	30.23	3.19	10.92	7.56	3.42
Dec. 2009 (-AO)	**-3.41**	**0**	**29.41**	**1.46**	**12.48**	**9.48**	**8.55**
Rubicon Peak (39.00°N, -120.14°W)							
	AO Value	# of ROS	Avg. Temp. (°F)	Total Precip. (in)	SWE Increase (in)	SWE Decrease (in)	SWE Increase/ Total Precip.
Dec. 2006 (+AO)	2.28	6	33.57	3.9	7.1	3.7	1.82
December 2018	0.11	3	31.78	2.6	9	7.4	3.46
Dec. 2009 (-AO)	**-3.41**	**11**	**29.20**	**6.4**	**14.5**	**7.9**	**2.27**
Carson Pass (38.69°N, -120.00°W)							
	AO Value	# of ROS	Avg. Temp. (°F)	Total Precip. (in)	SWE Increase (in)	SWE Decrease (in)	SWE Increase/ Total Precip.
Dec. 2006 (+AO)	2.28	7	29.68	5	9.8	4.4	1.96
Dec. 2018	0.11	8	27.68	2.5	10.3	7.3	4.12
Dec. 2009 (-AO)	**-3.41**	**2**	**25.55**	**6.1**	**12.4**	**5.6**	**2.03**
Charlotte Lake (36.78°N, -118.43°W)							
	AO Value	# of ROS	Avg. Temp. (°F)	Total Precip. (in)	SWE Increase (in)	SWE Decrease (in)	SWE Increase/ Total Precip.
Dec. 2006 (+AO)	2.28	0	22.77	4.4	5.04	1.08	1.15
Dec. 2018	0.11	96	21.18	2.41	10.01	9.91	4.15
Dec. 2009 (-AO)	**-3.41**	**0**	**14.16**	**7.99**	**6.6**	**0.12**	**0.83**

3.3.2. Change in SWE in association with temperature, SLP, and AO

As mentioned in section 3.3.1, there were no clear correlation between AO and temperature over a longer time periods, although there are some strong associations visible in Fig. 18 for some time period. Thus, in this section, we aim to look further at the SWE anomaly/AO and SWE anomaly/850 hPa temperature anomaly patterns. Figure 20 shows the correlations plots of SWE anomaly with AO and 850 hPa temperature anomaly during three different time periods (1988-1992, 2002-2006, and 2012-2016). They are negatively correlated for all periods over Northern California, although the significance varies, and the coefficient is higher in the recent time period (Fig. 20c). For example, when the warming and drought conditions were persistent, the maximum temperature anomaly was greater than 5 K and the maximum SWE loss was greater than 25 inches in the 2012-2016 period as shown in Fig. 18b. Although the overall relationship between SWE anomaly and AO index is not as robust as the relationship between SWE anomaly and the temperature anomaly, the positive AO index tends to be associated with the lower SWE.

This negative correlation has been more accelerated in the 2010s than the 1990s as the temperature anomaly and SWE anomaly has gotten higher (Figs. 18b, 20a and 20c). Although the overall significance is lower compared to that for the few time periods, this shows the recent conditions like extreme heat, surface warming, and severe drought may enhance the SWE loss in northern California. Indeed, the lower layer mean temperature, represented by the thickness between 500 hPa and 1000 hPa, shows a positive warm anomaly trend that is becoming more intense in recent years, as seen in Fig. 21.

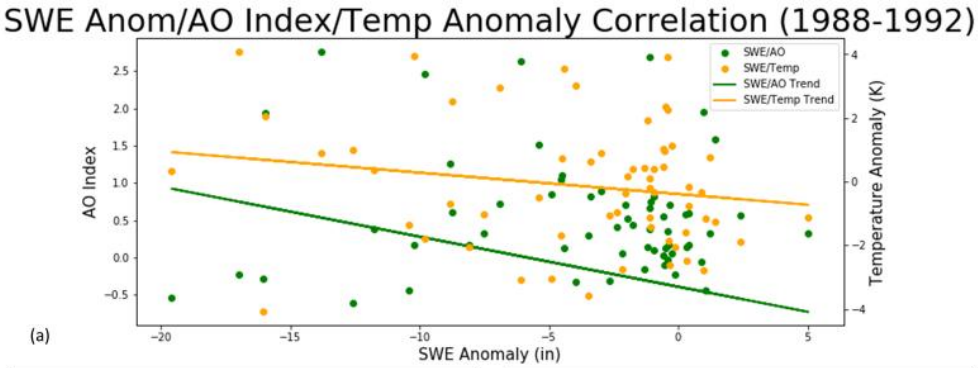

SWE Anomaly/ AO Index			
R-value:	0.063	P-value:	0.648

SWE Anomaly/ Temp Anomaly			
R-value:	0.184	P-value:	0.160

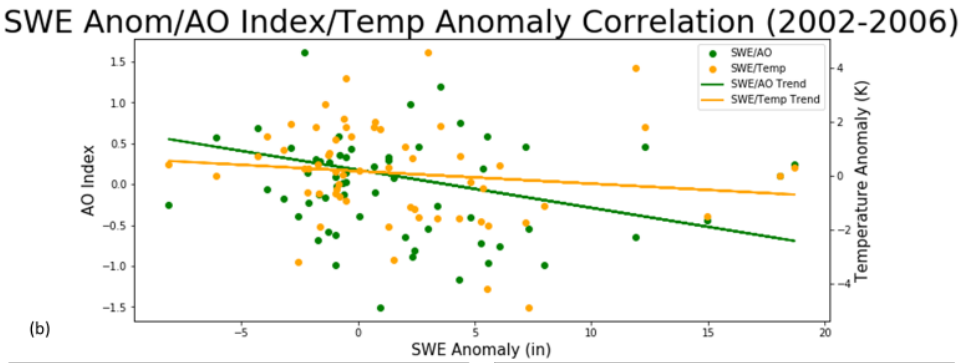

SWE Anomaly/ AO Index			
R-value:	0.130	P-value:	0.327

SWE Anomaly/ Temp Anomaly			
R-value:	0.184	P-value:	0.305

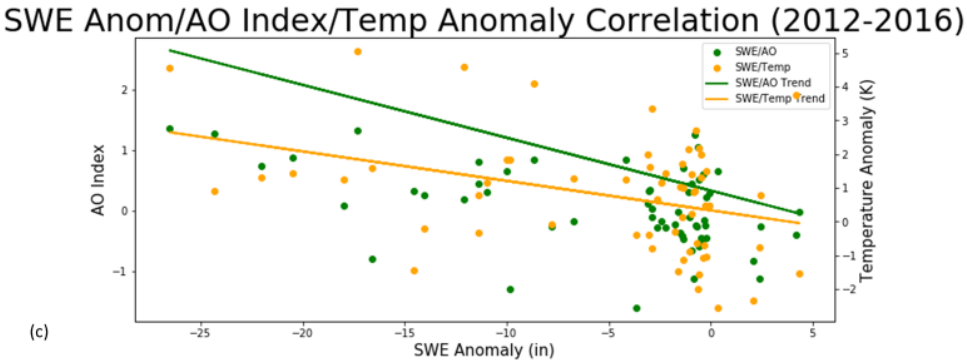

SWE Anomaly/ AO Index			
R-value:	0.445	P-value:	<0.000

SWE Anomaly/ Temp Anomaly			
R-value:	0.371	P-value:	0.004

Fig. 20. Scatter plot and trend lines for Northern California SWE anomaly as compared to the 3-month average AO Index and 850 hPa temperature anomaly for three different time periods.

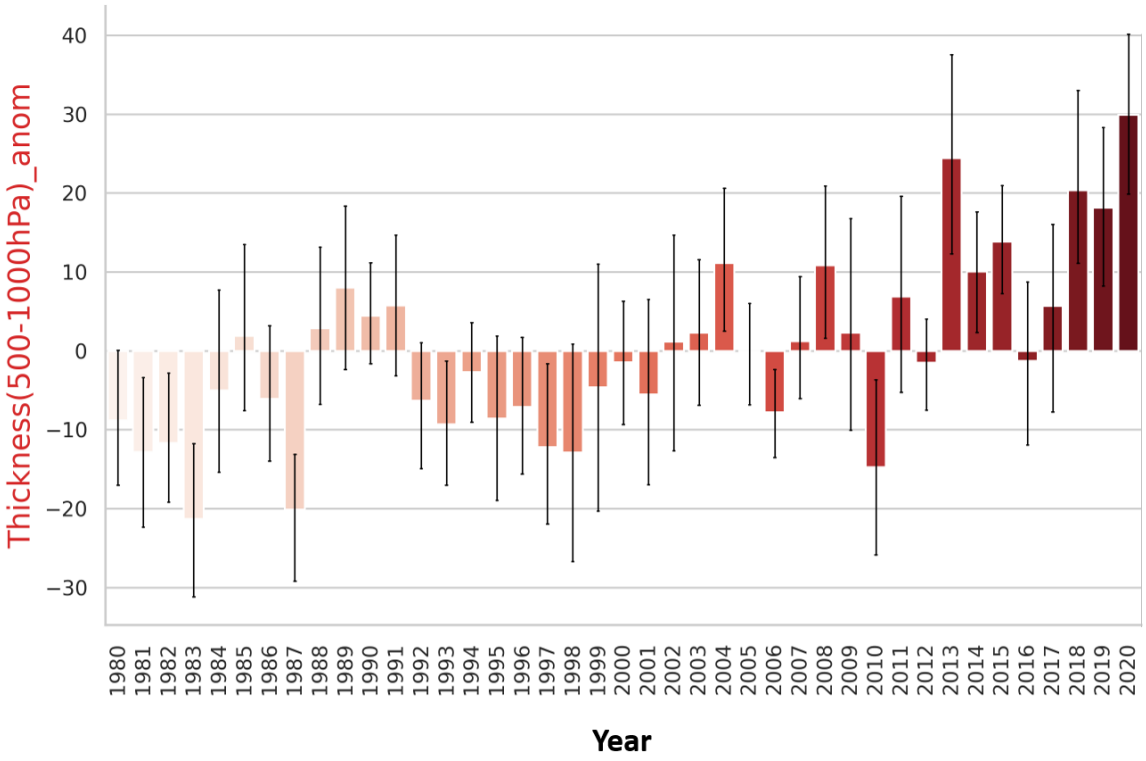

Fig. 21. Time series of thickness (geopotential height difference from 500 hPa to 1000 hPa) anomaly over the eastern Pacific and western U.S. (160-100 °W and 30-50 °N) from 1980 to 2020 obtained from MERRA2 data. The monthly data is averaged per year. The error bar represents the data within 95% confidence interval per year. The anomaly is calculated from the monthly data subtracting climatological mean (1980-2020) data.

The atmospheric variables such as SLP, lower layer mean temperature (i.e., lowermost layer between 500-1000 hPa), and low-level stability (LTS; defined by the difference in potential temperature from 700 hPa to 1000 hPa) are shifted to be positive in recent years, as shown in Fig. 22. While the trend of AO is not clearly observed (not shown), AO is positively correlated with the SLP anomaly and the temperature anomaly (Fig. 20), and the positive AO phase has been more frequent in recent years (e.g., years after 2008). Considering that SWE tends to be reduced in the positive AO phase and warmer lower atmospheric temperatures (at 850 hPa; see Fig. 20), we can also assume that this indicates

SWE may decrease if this condition persists. With this assumption, this analysis suggests AO along with SLP and low-level temperature may be used as useful metrics to help forecast and predict SWE in the northern California. Furthermore, while SWE-temperature-AO is negatively associated over northern California at a monthly time scale, the understanding of the regional differences in these relationships or at the different time scales (daily or weekly and synoptic time scale) and their impacts still have a room for improvement and need further investigation.

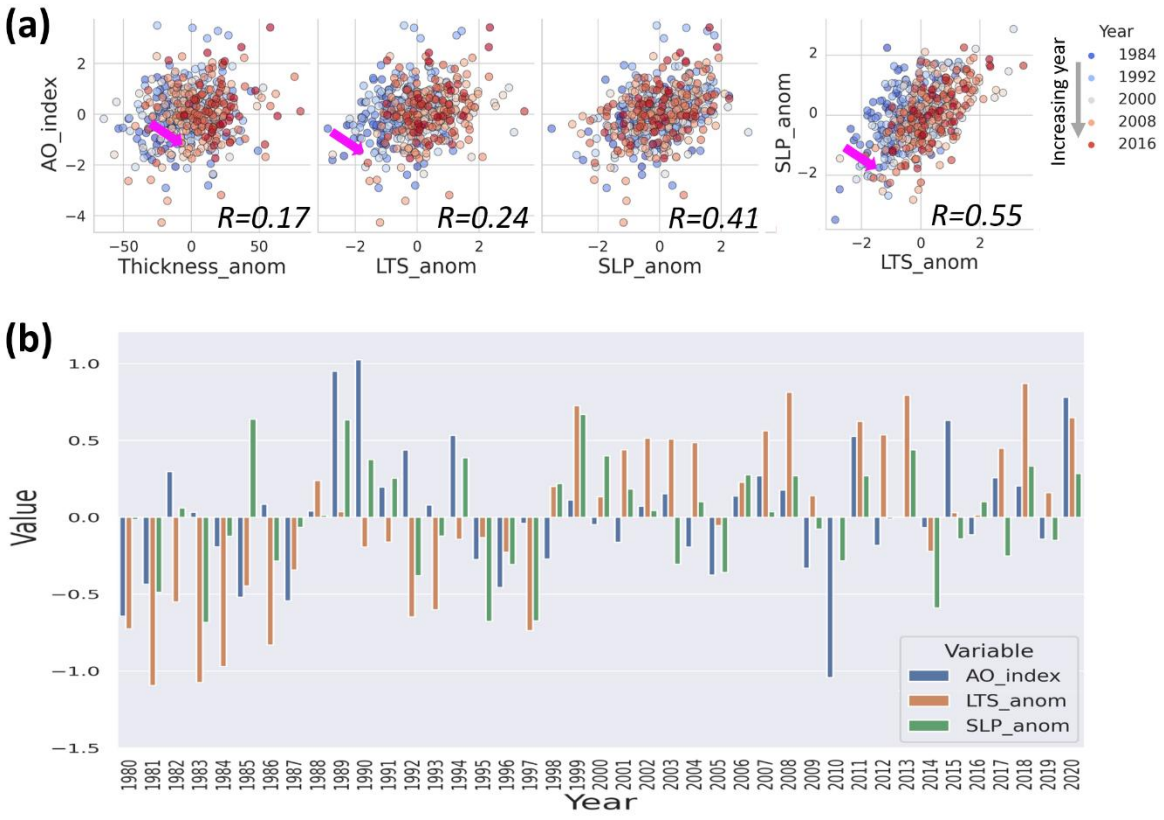

Fig. 22. (a) Scatter plots of AO index with thickness (geopotential height from 500 to 1000 hPa) anomaly, low-level tropospheric stability (LTS; potential temperature difference between 700 hPa and 1000 hPa) anomaly, and SLP anomaly. Scatter plot of SLP anomaly with LTS anomaly. The anomaly is calculated from monthly data subtracted by climatological mean (1980-2020). The SLP anomaly is normalized by subtracting climatological mean from each value and dividing by their standard deviation. (b) Time series of AO, LTS anomaly, and the normalized SLP anomaly over the eastern Pacific and western U.S. (160-100 °W and 30-50 °N) from 1980 to 2020 obtained from MERRA2 data. The monthly data is averaged per year. The R-values in (a) represents the Pearson correlation (with p-value < 0.01). The data includes all the monthly data from 1980 to 2020. The magenta arrow in (a) represents the shifted pattern over time.

4. Discussion and Conclusion

We investigated how the synoptic and large-scale conditions are shaped by Arctic Oscillation (AO), and how they are associated with different characteristics of atmospheric rivers (ARs), particularly focusing on the northwestern U.S. during Northern Hemisphere winter for forty years (1980 – 2019). To determine the effect of climate conditions measured in the AO index on weather events, we compared the two opposing phases. We started this study by first examining the synoptic conditions of the positive and negative phases of AO such as SLP, geopotential height, and wind speed. This established the different synoptic atmospheric conditions of the phases and how they relate to ARs. Next, the AR characteristics such as intensity, duration, and frequency relative to the years that we investigated were compared in the different phases of AO. With these variances established the next phase was to analyze how they translated to precipitation with GPM and MERRA2 IVT measurements. Lastly, we examined case studies to investigate associations of California mountain snowpack and rain-on-snow (ROS) events with AO phases in conjunction with other environmental factors such as temperature.

In summary, part one of our study demonstrated that the synoptic conditions of the negative phase of Arctic Oscillation allows for more upper-level wavelike patterns in the northern Pacific region with stronger low-level jet, transporting more moisture to the western U.S. and that the positive phase had the opposite conditions. Part two showed quantitatively that the negative AO months from 1980 through 2019 had higher AR IVT, longer duration and more ARs per month than average and that the positive AO months had

lower IVT, shorter ARs and less ARs per month than average, over the six local regions of the western U.S. In part three, we illustrated how IVT, and precipitation could possibly be related to the AO phase, however due to high variability a clear conclusion for this could not be reached so other factors must also be responsible which would require further investigation. Lastly, our case study determined no strong connection between the AO and ROS, although some linkage between low SWE and high temperatures are found during the positive AO phase. No clear relationship between ROS and AO during the entire time period may also be related to the limitation of the use of the different spatial and coarse temporal resolution (monthly mean) data, which may not capture the synoptic variability during ARs. However, the negative correlation between AO and temperature and AO and SWE in the selected time periods were more statistically significant and stronger in recent years.

This study highlights the synoptic conditions shaped by the different phases of climate variability, such as AO, has a different impact on the characteristics of extreme precipitation events, like ARs, and snowpack over the local region. While more reduction of SWE is projected if the warmer low-level temperature and higher SLP trends persist, implementing more observation sites or considering other guiding elements will be beneficial to better understand possible controlling factors on snowpack during extreme events like ARs in the warming climate.

References

American Meteorological Society, 2020: atmospheric river. Accessed May 29 2020 https://glossary.ametsoc.org/wiki/Atmospheric_river. © American Meteorological Society. Used with permission.

Brill, K. F., L. W. Uccellini, R. P. Burkhart, T. T. Warner, and R. A. Anthes, 1985: Numerical Simulations of a Transverse Indirect Circulation and Low-Level Jet in the Exit Region of an Upper-Level Jet. *Journal of J. Atmos. Sci.,* **42**, 1306-1320, https://doi.org/10.1175/1520-0469(1985)042<1306:NSOATI>2.0.CO;2.

Department of Water Resources, 2021: CDEC Webservice JSON and CSV. California Data Exchange Center, Accessed September 11, 2021, https://cdec.water.ca.gov/dynamicapp/wsSensorData.

Dettinger, M. D., 2013: Atmospheric rivers as drought busters on the US West Coast. *J. Hydrometeor.*, **14**, 1721-1732, https://doi.org/10.1175/JHM-D-13-02.1.

Dettinger, M. D., F. M. Ralph, T. Das, P. J. Neiman, and D. R. Cayan, 2011: Atmospheric rivers, floods and the water resources of California. *Water*, **3**, 445-478, https://doi.org/10.3390/w3020445.

Goldenson, N., L. R. Leung, C. M. Bitz, and E. Blanchard-Wrigglesworth, 2018: Influence of atmospheric rivers on mountain snowpack in the western United States. *J. Climate* , **31**, 9921–9940. https://doi.org/10.1175/JCLI-D-18-0268.1.

Guan, B., N. P. Molotch, D. E. Waliser, E. J. Fetzer, and P. J. Neiman, 2013: The 2010/2011 snow season in California's Sierra Nevada: Role of atmospheric rivers and modes of large-scale variability. *Water Resour. Res.*, **49**, 6731–6743, https://doi.org/10.1002/wrcr.20537.

Guan, B., and D. E. Waliser, 2015: Detection of atmospheric rivers: Evaluation and application of an algorithm for global studies. *J. Geophys. Res. Atmos.*, **120**, 12514-12535, https://doi.org/10.1002/2015JD024257.

Guan, B., D. E. Waliser, F. M. Ralph, E. J. Fetzer, and P. J. Neiman, 2016: Hydrometeorological characteristics of rain-on-snow events associated with atmospheric rivers. *Geophys. Res. Lett.*, **43**, 2964–2973, https://doi.org/10.1002/2016GL067978.

Harris, S. M., and L. M. V. Carvalho, 2018: Characteristics of southern California atmospheric rivers. *Theor. Appl. Climatol.*, **132**, 965–981, https://doi.org/10.1007/s00704-017-2138-1.

Kim, S., and J. C. Chiang, 2021: Atmospheric River Lifecycle Characteristics Shaped by Synoptic Conditions at Genesis. *Int. J. of Climatol*., 1-18, https://doi.org/10.1002/joc.7258.

Matsuo, K., and K. Heki, 2012: Anomalous precipitation signatures of the Arctic Oscillation in the time-variable gravity field by GRACE. *Geophys. J. Int.*, **190**, 1495–1506, https://doi.org/10.1111/j.1365-246X.2012.05588.x.

McCabe-Glynn, S., K. R. Johnson, C. Strong, Y. Zou, J. Y. Yu, S. Sellars, and J. M. Welker, 2016: Isotopic signature of extreme precipitation events in the western U.S. and associated phases of Arctic and tropical climate modes. *J. Geophys. Res. Atmos.*, **121**, 8913–8924, https://doi.org/10.1002/2016JD025524.

NASA Goddard Space Flight Center, 2017: Atmospheric River Slams California. National Aeronautics and Space Administration, Accessed October 16, 2021, https://gpm.nasa.gov/science/atmospheric-river-slams-california.

National Centers for Environmental Information, 2021: Arctic Oscillation (AO) National Oceanic and Atmospheric Administration. Retrieved February 9 2021, https://www.ncdc.noaa.gov/teleconnections/ao/.

Neiman, P. J., F. M. Ralph, G. A. Wick, J. D. Lundquist, and M. D. Dettinger, 2008: Meteorological characteristics and overland precipitation impacts of atmospheric rivers affecting the West Coast of North America based on eight years of SSM/I satellite observations. *J. Hydrometeor.*, **9**, 22-47, https://doi.org/10.1175/2007JHM855.1.

Newell, R. E., N. E. Newell, Y. Zhu, and C. Scott, 1992: Tropospheric rivers?–A pilot study. *Geophys. Res. Lett.*, **19**, 2401-2404, https://doi.org/10.1029/92GL02916.

Ralph, F. M., T. Coleman, P. J. Neiman, R. J. Zamora, and M. D. Dettinger, 2013: Observed impacts of duration and seasonality of atmospheric-river landfalls on soil moisture and runoff in coastal northern California. *J. Hydrometeor.,* **14**, 443-459, https://doi.org/10.1175/JHM-D-12-076.1.

Ralph, F. M., and M. D. Dettinger, 2011: Storms, floods, and the science of atmospheric rivers. *Eos Trans. AGU*, **92**, 265-266, https://doi.org/10.1029/2011EO320001.

Ralph, F. M., and Coauthors, 2017: Dropsonde observations of total integrated water vapor transport within North Pacific atmospheric rivers. *J. Hydrometeor.,* **18**, 2577-2596, https://doi.org/10.1175/JHM-D-17-0036.1. © American Meteorological Society. Used with permission.

Ralph, F. M., J. J. Rutz, J. M. Cordeira, M. D. Dettinger, M. Anderson, D. Reynolds, L. J. Schick, and C. Smallcomb, 2019: A scale to characterize the strength and impacts of atmospheric rivers. *Bull. Amer. Meteor. Socy.,* **100**, 269–289, https://doi.org/10.1175/BAMS-D-18-0023.1.

Rutz, J. J., James, W. Steenburgh, and F. M. Ralph, 2014: Climatological characteristics of atmospheric rivers and their inland penetration over the western United States. *Mon. Wea. Rev.*, **142**, 905–921, https://doi.org/10.1175/MWR-D-13-00168.1.

Ryoo, J. M., Y. Kaspi, D. W. Waugh, G. N. Kiladis, D. E. Waliser, E. J. Fetzer, and J. Kim, 2013: Impact of Rossby wave breaking on US West Coast winter precipitation during ENSO events. *J. Climate ,* **26**, 6360-6382, https://doi.org/10.1175/JCLI-D-12-00297.1.

Ryoo, J. M., D. E. Waliser, D. W. Waugh, S. Wong, E. J. Fetzer, and I. Fung, 2015: Classification of atmospheric river events on the US West Coast using a trajectory model. *J. Geophys. Res. Atmos.,* **120**, 3007-3028, https://doi.org/10.1002/2014JD022023.

Ryoo, J. M., and Coauthors, 2020: Terrain trapped airflows and precipitation variability during an atmospheric river event. *J. Hydrometeor.,* **21**, 355-375, https://doi.org/10.1175/JHM-D-19-0040.1.

Scherrer, S. C. 2020: Temperature monitoring in mountain regions using reanalyses: Lessons from the Alps. *Environ. Res. Lett.*, **15**, 1-9, https://doi.org/10.1088/1748-9326/ab702d.

Thompson, D. W. J., and J. M. Wallace, 1998: The Arctic oscillation signature in the wintertime geopotential height and temperature fields. *Geophysical Research Letters*, **25**, 1297–1300, https://doi.org/10.1029/98GL00950.

Zechiel, P. R., and S. Chiao, 2021: Climate Variability of Atmospheric Rivers and Droughts over the West Coast of the United States from 2006 to 2019. *Atmosphere*, **12**, 1-20, https://doi.org/10.3390/atmos12020201.

Zhu, Y., and R. E. Newell, 1994: Atmospheric rivers and bombs. *Geophys. Res. Lett.*, **21**, 1999-2002, https://doi.org/10.1029/94GL01710.

Zhu, Y., and R. E. Newell, 1998: A proposed algorithm for moisture fluxes from atmospheric rivers. *Mon. Wea. Rev.*, **126**, 725–735, https://doi.org/10.1175/1520-0493(1998)126<0725:APAFMF>2.0.CO;2.